Huaijun Wang
Marie Van de Putte
Feng Chen
Frederik De Keyzer
Lixin Jin
Jie Yu
Guy Marchal
Peter de Witte
Yicheng Ni

Murine liver implantation of radiation-induced fibrosarcoma: characterization with MR imaging, microangiography and histopathology

H. Wang · F. Chen · F. De Keyzer ·
L. Jin · J. Yu · G. Marchal · Y. Ni (✉)
Department of Radiology,
University Hospitals,
Catholic University of Leuven,
Herestraat 49,
3000 Leuven, Belgium
e-mail: Yicheng.Ni@med.kuleuven.be
Tel.: +32-16-330165
Fax: +32-16-343765

M. Van de Putte · P. de Witte
Laboratory for Pharmaceutical Biology,
Faculty of Pharmaceutical Sciences,
K.U. Leuven,
Herestraat 49,
3000 Leuven, Belgium

F. Chen
Department of Radiology, Zhong Da
Hospital, Southeast University,
87 Ding Jia Qiao Road,
Nanjing, 210009, Jiangsu Province,
China

Abstract We sought to establish and characterize a mouse liver tumor model as a platform for preclinical assessment of new diagnostics and therapeutics. Radiation-induced fibrosarcoma (RIF-1) was intrahepatically implanted in 27 C3H/Km mice. Serial in vivo magnetic resonance imaging (MRI) with a clinical 1.5-T-magnet was performed using T1- (T1WI), T2- (T2WI), and diffusion-weighted sequences (DWI), dynamic contrast-enhanced MRI (DCE-MRI), and contrast-enhanced T1WI, and validated with postmortem microangiography and histopathology. Implantation procedure succeeded in 25 mice with 2 deaths from overdosed anesthesia or hypothermia. RIF-1 grew in 21 mice with volume doubling time of 2.55 ± 0.88 days and final size of 216.2 ± 150.4 mm^3 at day 14. Three mice were found without tumor growth and one only with abdominal seeding. The intrahepatic RIF-1 was hypervascularized with negligible necrosis as shown on MRI, micro-angiography and histology. On DCE-MRI, maximal initial slope of contrast-time curve and volume transfer constant per unit volume of tissue, K, differed between the tumor and liver with only the former significantly lower in the tumor than in the liver ($P<0.05$). Liver implantation of RIF-1 in mice proves a feasible and reproducible model and appears promising for use to screen new diagnostics and therapeutics under noninvasive monitoring even with a clinical MRI system.

Keywords Mouse · Neoplasm · Liver · Animal model · MR imaging

Introduction

Breakthroughs in cancer research often rely upon advances made with experimental animal models. Appropriate tumor models not only empower our comprehension of in vivo biology including tumor initiation, promotion, progression, and metastasis, but also facilitate more clinically relevant applications, including selection, identification, and validation of biomarkers for cancer diagnosis and evaluation of newly developed agents or methods for cancer therapies [1].

Owing to favorable cost-effectiveness and relatively easy management, mouse models of malignancy have been most widely used and proven immensely valuable in cancer research [1, 2]. These tumor models can be derived through spontaneous occurrence, chemical or physical induction by carcinogens or radiations, inoculation or implantation with tumor cell suspension or tissue fragment, as well as genetic manipulations by gene knockin or knockout [1, 2].

Most of the tumor models with allograft or xenograft implantation are preferentially made at subcutaneous locations due to the convenient operation and observation [3–7]. Subcutaneously implanted radiation-induced fibrosarcoma (RIF-1) has been one of the most widely used mouse tumor models in cancer research for its biological

stability, minimal immunogenicity, low metastatic potential, and responsiveness to various therapeutic interventions [8].

However, the majority of malignant tumors found in clinical patients are located deeply in visceral organs, which considerably differ from superficial tumors in terms of blood supply, biological behavior, and therapeutic response. Thus, experimental tumor growth in visceral organs has been regarded more clinically relevant [9–11].

The liver is the largest internal organ that not only generates various primary tumors of hepatic origin, such as hepatocellular carcinoma and cholangiocarcinoma, but also harbors secondary tumors, e.g., liver metastasis of colorectal cancer, through its abundant blood supply and lymph drainage [10, 11]. Therefore, tumor implantation in the liver is more popular than that in other organs for various research topics [9–11]. But, to our knowledge, liver implantation of RIF-1 tumor in the mouse has never been reported.

Compared to subcutaneous implantation, one major disadvantage of visceral tumor models is the difficult access to tumor for noninvasive and longitudinal investigations. Thanks to recent advances in imaging technology, powerful techniques, such as computed tomography (CT) and magnetic resonance imaging (MRI), have become widely available in clinic to demonstrate 2D and 3D high-resolution images integrating both morphological and functional information. Furthermore, modern cell biology and molecular medicine have prompted miniaturization of these imaging modalities into micro-CT and MR micorscopy as nondestructive monitoring tools in life sciences for imaging small animals, such as mice [6, 7, 12, 13]. However, all these dedicated equipments are extremely expensive and virtually unavailable to many clinic-based researchers, an obstacle that needs to be circumvented.

It was under such a circumstance that we initiated the present experiment with the following working hypotheses: (1) the implantation of RIF-1 tumor into the liver could be feasible and reproducible in mice for further clinically relevant studies; (2) this liver tumor model could be noninvasively monitored and characterized using a clinical 1.5-T MR scanner; (3) in vivo imaging findings could be further validated by postmortem gold standard methods. In addition, this experimental setting may prove useful for those academic clinicians who are interested in using mice for their cancer research, but have the access only to clinical imagers.

Materials and methods

Tumor model

This study protocol was compliant with our current institutional regulations for use and care of laboratory animals.

The C3H/Km mice weighing about 20 g were purchased from Charles River Laboratory, France. Radiation-induced fibrosarcoma (RIF-1) cell line was obtained from the Netherlands Cancer Institute, the Netherlands, and maintained through consecutive allograft by the laboratory of pharmaceutical biology in our institute. One mouse with a RIF-1 tumor growing on the dorsum served as a tumor donor. Liver implantation of RIF-1 tumor was performed in 27 mice of the same strain according to a method introduced for rats [9]. Briefly, after anesthesia with intraperitoneal injection of 1.0 ml/kg of pentobarbital (Nembutal; Sanofi Sante Animale, Brussels, Belgium), the hair on the abdomen was removed, and midline laparotomy was performed. A small incision was made on left liver lobe, and a piece of gelatine sponge was filled in for temporal hemostasis. Then a fragment of RIF-1 tumor about 1–2 mm^3 was inserted to replace the sponge, and a droplet of tissue glue (Histoacryl; Aesculap, Tuttlingen, Germany) was applied to seal the incision. Finally, the abdomen was closed by layered sutures, and the mouse was placed on a heating pad until recovery from anesthesia.

Study protocol

All mice were examined with MRI at 7, 10, 12, and 14 days after tumor implantation. For the follow-up at 14 days, the MRI protocol included T1-weighted imaging (T1WI), T2-weighted imaging (T2WI), diffusion-weighted imaging (DWI), dynamic contrast-enhanced MRI (DCE-MRI), and contrast-enhanced T1WI (CE-T1WI). For the follow-up at 7, 10, and 12 days, only T1WI, T2WI, and DWI were performed. All animals were killed for postmortem examinations after the last MRI session.

MR imaging

Under gas anesthesia of 2% isoflurane in the mixture of 20% oxygen and 80% room air, the mouse was placed supinely in a plastic holder with a tube connected to a gas anesthesia system (Harvard Apparatus, Holliston, MA), which was located outside of the MR scanning room. The tail vein was cannulated for the injection of contrast agent.

MR imaging was performed with a 1.5-T whole-body MR imager (Sonata; Siemens, Erlangen, Germany) of a 40 mT/m maximum gradient capacity with a small flex loop coil of 4-cm diameter (Siemens, Erlangen, Germany), with the body coil serving as the transmitter coil.

Sagittal, coronal, and axial pilot images were first obtained for localizing the subsequent MRI acquisitions.

For each imaging sequence except DCE-MRI, 12 axial and 6 coronal images were acquired with a slice thickness of 2 mm with a 0.4-mm slice gap. For spin-echo (SE) T1WI, the images were acquired with repetition time/echo time (TR/TE) of 500/15 ms, field of view (FOV) of

28×44 mm, image acquisition matrix of 240×512, and thus the in-plane resolution of 0.12×0.09 mm. Four scans were averaged to obtain an improved signal-to-noise ratio, which led to a total scanning time of 4 min 50 s.

For turbo SE (TSE) T2WI, the images were acquired with TR/TE of 3,000/71 ms, FOV of 25×44 mm, acquisition matrix of 111×256, turbo factor of 11, and thus the in-plane resolution of 0.23×0.17 mm. Six acquisitions led to a total data acquisition time of 3 min 41 s.

For DWI, the images were acquired by using a two-dimensional single-shot TSE sequence (haste-diffusion) with TR/TE of 2,650/105 ms, FOV of 56×100 mm and acquisition matrix of 108×256. The latter two parameters led to an in-plane resolution of 0.52×0.39 mm. Four acquisitions led to the total data acquisition time of 1 min 4 s. Diffusion gradients were applied along the read direction with b value of 100 s/mm^2.

For DCE-MRI, the axial images were acquired by using a three-dimensional T1-weighted gradient-echo sequence (volumetric interpolated breathhold examination or VIBE) of fat saturation, with TR/TE of 7.2/2.83 ms, FOV of 49×120 mm, flip angle of 10°, acquisition matrix of 166×512 and voxel size 0.30×0.23×2.4 mm, but without breathholding. The dynamic image series of 60 measurements (12 images for 1 measurement of 3.8 s and 720 images in total) led to a total scanning time of 3 min 49 s. During the dynamic sequence, gadodiamide (Omniscan; Amersham, Oslo, Norway) with a gadolinium concentration of 0.5 mol/l was injected intravenously at a dose of 0.01 mmol/kg in total volume of 0.06 ml diluted with saline. After the 15th measurement to ensure a sufficient precontrast baseline, the bolus injection was administrated manually via tail vein within less than 1 s without saline flush.

Immediately after DCE-MRI was finished, gadodiamide was intravenously injected again at a dose of 0.1 mmol/kg in total volume of 0.06 ml diluted with saline for acquiring CE-T1WI.

Digital microangiography and histological analysis

Immediately after the last MRI session at 14 days after implantation, the mice were killed with an intravenous overdose of pentobarbital. For postmortem verification of tumor, we applied the following macro- and microscopic procedures.

Briefly, after laparotomy, abdominal aorta and portal vein were cannulated. To determine the source of blood supply to a tumor, barium suspension (Micropaque; Guerbet, Roissy, Cedex, France) was first injected through the abdominal aorta until the appearance of barium in distal capillaries, followed by dissection of the entire tumor bearing liver. Using a digital mammographic unit (Embrace; Agfa-Gevaert, Mortsel, Belgium) at 25 kV and 6 mAs, hepatic arteriography was made prior to stepwise

portovenography until complete filling of the portal vein branches with barium suspension. The injected barium particles served also as a green-yellowish intravascular marker in microscopic preparations.

After the microangiography, the liver specimens were fixed in 10% formalin and processed with paraffin sections and hematoxylin-eosin staining to correlate histomorphological features of RIF-1 tumor with MRI findings.

Imaging analysis

Tumor growth All the analyses, except DCE-MRI, were performed using the built-in software of the MRI system with a consensus by three experienced radiologists. The tumor was delineated on each tumor-containing image of T2WI by using an operator-defined region of interest (ROI). The area of tumor was automatically generated, and the total area of tumor was multiplied by the thickness plus gap to obtain the volume of tumor. The doubling time (DT) of tumor volume was calculated with the following equation: $DT = (T - T_0) \log 2/(\log V - \log V_0)$, where $T-T_0$ indicates the length of time between two measurements, and V_0 and V denote the tumor volume at two consecutive points of measurement [14].

Signal intensity The tumor was delineated as a ROI on the image containing the tumor of greatest area on T1WI and CE-T1WI. The signal intensity (SI) of tumor was automatically generated.

DCE-MRI The analysis of DCE-MRI was performed off-line at a workstation by using dedicated LINUX-based software (Biomap; Novartis, Basel, Switzerland). Briefly, contrast-time curve (CTC) maps were calculated from the dynamic perfusion images with the assumption of a linear relation between the amount of contrast agent in the tissue and the resulting difference in relaxation time, which is true when low doses of a gadolinium-based contrast agent are used [15]. Then, on DCE-MRI source images, the tumor was delineated on the image containing tumor of greatest area, a circular ROI about 17 mm^2 was drawn on normal liver tissue, and arterial input function was assessed by placing an additional ROI in the abdominal aorta for detecting the presence of gadodiamide in the blood plasma. The three ROIs were copied and pasted onto the resultant CTC map to calculate the volume transfer constant per unit volume of tissue, K, in tumor and normal liver tissue by fitting the Tofts and Kermode model. K, instead of more popular denotation K^{trans}, was used here with the assumption that permeability of tumor vessels for contrast agent flow from intravascular to extracellular extravascular space is identical to their permeability for flow from extracellular extravascular to intravascular space [16, 17]. The maximal initial slope of CTC was

also generated at the two consecutive time points of maximal concentration change of contrast.

Statistical analysis

Statistical analysis was performed by using Excel 13.0. Numeric data were reported as means ± standard deviations (SD). Paired and two-tailed Student's t test was used to compare the different MRI parameters between tumor and normal liver tissues for different MRI techniques. Statistical difference was indicated if P was less than 0.05.

Testing the usefulness of model

In our ongoing research, the therapeutic effect of an anti-tubulin vascular targeting agent or VTA (combretastatin A-4 phosphate; OXiGENE, Watertown, MA), as iv administered at 5 mg/kg, has been successfully evaluated with the present experimental setting, i.e., the murine model of intrahepatic RIF-1 tumor implantation plus the above-described MRI protocol.

Results

General conditions

All mice survived the operational procedures except two: one died of an overdose of pentobarbital during the anesthesia; the other died of hypothermia during surgery. At 14 days after the implantation, all alive mice (n=25) appeared normal without pallor, piloerection, aggression, restlessness, weakness, tremors, diarrhea, ascites, and loss of hair or appetite.

Tumor growth

Among the 25 mice, there was no apparent hepatic RIF-1 tumor growth in three mice during the 14-day post-implantation period, and one mouse was found only with an intraperitoneal tumor. In the rest of the 21 mice, the tumor growth was slow during the first 7 days and accelerated afterwards, reaching the size over 5.0 mm in diameter at 14 days after implantation with averaged tumor volume of 216.2±150.4 mm^3 (Fig. 1), a size easily detectable with clinical imagers and applicable for further studies. The growing speed of tumor varied among individuals as reflected by extensive standard deviations (Fig. 1). Tumor doubling time was 2.55±0.88 days during the first 14 days.

Morphological MRI findings

As spheroid intrahepatic nodules, all tumors appeared homogenously hyperintense on T2WI (Fig. 2a,a') and slightly hypointense or isointense on T1WI (Fig. 2b,b'). On CE-T1WI, homogeneous contrast enhancement of tumor was observed (Fig. 2c,c'), suggesting hypervascularity of RIF-1 liver growth. DWI depicted the tumor as a hyperintense nodule (Fig. 2d,d'). In three tumors, minute necrosis was detected in the center with lower SI on T1WI and higher SI on T2WI and DWI relative to the viable part of the tumor. On CE-T1WI, contrast administration resulted in a nearly three-fold enhancement in SI of tumor from 418.4±115.9 arbitrary units (a.u.) to 1,128.7±325.8 a.u., in comparison to less than two-fold enhancement of normal liver from 386.2±134.2 a.u. to 663.9±210.1 a.u. ($P<0.01$).

Functional MRI findings

The patterns of DCE-MRI-derived CTC among tumor, normal liver and abdominal aorta were shown in Fig. 3. Compared with the earlier peak for abdominal aorta, the first-pass effect appeared almost simultaneously for tumor and normal liver with the maximal enhancement occurring at the same time and the maximal SI slightly greater in the liver than in tumor ($P>0.05$). DCE-MRI quantitatively demonstrated the SI changes over time. The maximal initial

Fig. 1 Tumor growth curve of RIF-1 tumor in mouse liver, from which the tumor volume doubling time of 2.55±0.88 days was derived. Error bars, ±SD
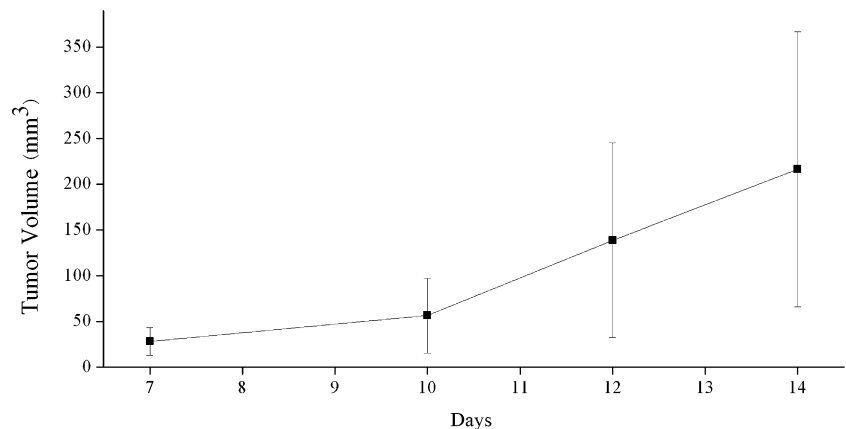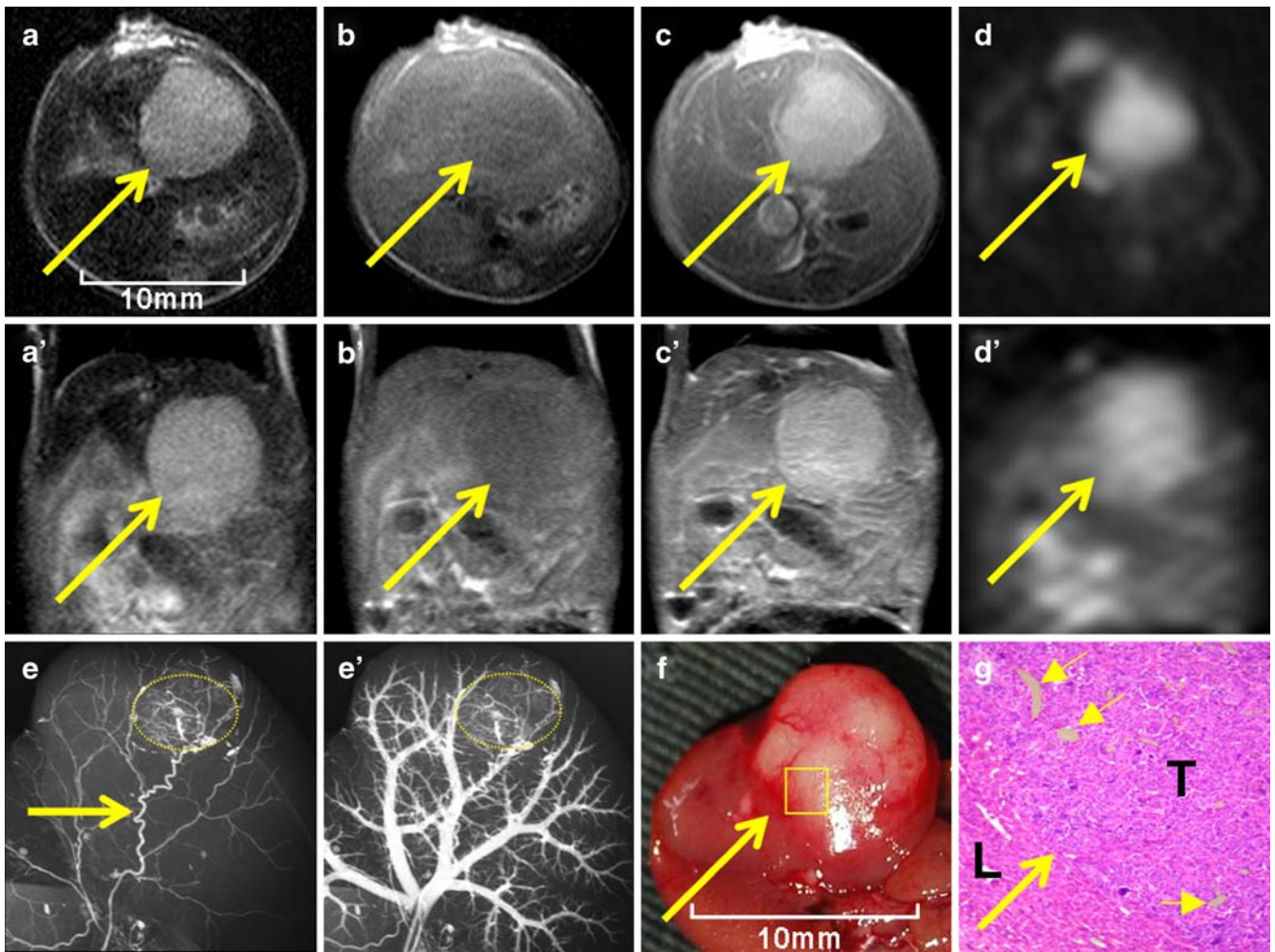
Fig. 2 Imaging findings of implanted RIF-1 tumor in murine liver. The spherical tumor (arrow) showed homogeneous abnormal signal intensity on axial T2WI (**a**), pre-contrast T1WI (**b**), contrast-enhanced T1WI (**c**), and DWI (**d**), and on corresponding coronal images (**a'**-**d'**). Digital microangiogram (**e** and **e'**) revealed irregular intratumoral vascularity (dashed circle). A torturous feeding artery (arrow) from the hepatic artery was shown on arterial phase (**e**). On portal venous phase (**e'**), branches of the portal vein in normal liver tissue were filled with barium, but the tumor showed a void of further barium filling, suggesting a sole arterial supply to the tumor. Photomacrograph (**f**) and photomicrograph (**g**) confirmed the solitary, homogeneous and malignant features of the RIF-1 tumor. Rectangular frame (**f**) denotes the area where microscopy was focused (**g**), which showed the border (arrow) between normal liver tissue (L) and tumor (T) as well as intratumoral vessels (small arrows) filled with barium (hematoxylin-eosin stain; original magnification ×100)

Fig. 3 Contrast-time curve (CTC) of abdominal aorta, normal liver, and RIF-1 tumor of all mice with averaged values at each time point during dynamic contrast-enhanced MRI (DCE-MRI). The first pass of contrast bolus arrived at the 15th measurement, and the curves rose abruptly within a few seconds after injection. There was no significant difference between the normal liver and RIF-1 tumor at each time point, suggestive of hypervascular nature of RIF-1 tumor. Error bars, ±SD
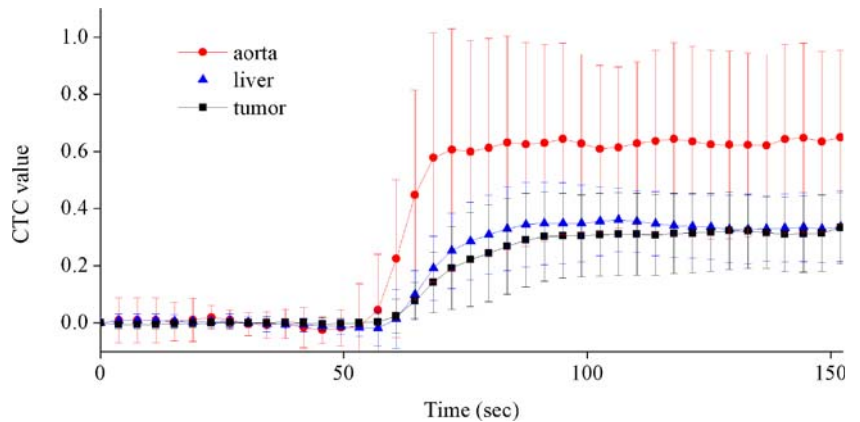
slope of CTC was 0.084±0.057 for tumor and 0.122±0.074 for normal liver (P=0.030). The volume transfer constant k was 0.174±0.172 sec^{-1} for tumor and 0.247±0.195 sec^{-1} for normal liver (P=0.096).

Postmortem microangiographic and histomorphologic findings

Microangiography revealed tortuous and dilated afferent arteries to all intrahepatic nodules with considerable intratumoral contrast staining at arterial phase, confirming well-developed vasculature of RIF-1 tumor in the liver (Fig. 2e), whereas portal venous branches ended up only in liver parenchyma, suggesting the sole arterial blood supply to implanted RIF-1 tumor (Fig. 2e'). Macroscopically, the intrahepatic RIF-1 mass grew in an expansion pattern against liver parenchyma with a paler color than surrounding normal liver (Fig. 2f). Photomicrograph demonstrated that 14 days after implantation, RIF-1 tumor cells looked either undifferentiated as small cells with large nuclei or poorly differentiated as spindle-shaped cells, both with numerous mitotic phases (Fig. 2g). Intratumoral foci of necrosis were occasionally observed.

Application examples

Using the present experimental setting, the dramatic effect of the VTA on destroying intratumoral vasculature in the RIF-1 tumor and posttherapeutic tumor relapse was successfully documented as exemplified in Fig. 4.

Discussion

Mouse liver tumor model

The present study demonstrates that RIF-1 liver implantation in mice as a model of solitary tumor in the visceral organ is feasible and reproducible with a growth rate over 84% (21/25) and mortality rate lower than 8% (2/27). To the best of our knowledge, it is the first time that a murine liver tumor model has been derived from RIF-1 tumor cell line after tissue fragment implantation. The tumor volume doubling time of 2.55 days for intrahepatic growth in the present study is somewhat shorter than the 2.7 days reported for subcutaneous RIF-1 tumor growth [8], which is reasonable if the diverse microenvironment and blood supply between the liver and connective tissue are taken
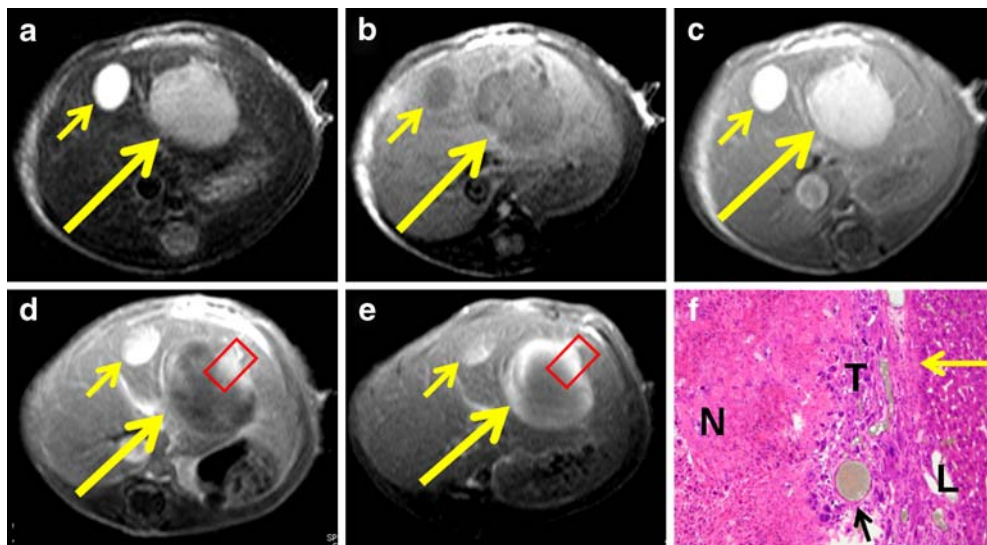

Fig. 4 Therapeutic effect of an anti-tubulin vascular targeting agent or VTA (combretastatin A-4 phosphate; OXiGENE, Watertown, MA) in a mouse with implanted liver RIF-1 tumor as monitored noninvasively with a 1.5-T clinical MRI unit. Plane T2WI (**a**), T1WI (**b**) and CE-T1WI (**c**) before therapy showed a spherical hyperintense, hypointense, and homogeneously hyperenhanced liver mass (arrow), respectively. The adjacent oval structure (small arrow) is the gall bladder. Two hours after iv injection of the VTA at 5 mg/kg in the same mouse, CE-T1WI showed a lack of CE in the tumor (arrow) except a strong focal CE at the upper left edge (**d**). Forty-eight hours after therapy, on CE-T1WI, the tumor (arrow) appeared unenhanced at the center, but surrounded by a strong rim CE (**e**). The red rectangular frames in D and E denote where microscopy was approximately focused. The photomicrograph (**f**) revealed that besides central massive necrosis (N), there was marginal tumor relapse corresponding to the strong rim CE (E), particularly near the tumoral afferent artery (black arrow), which was non-responsive to the effect of VTA, a potential reason why this type of therapeutics normally do not show curative effects. The yellow arrow points to the border between normal liver tissue (L) and tumor (T) (hematoxylin-eosin stain; original magnification ×100)

into account. Liver is a typical hypervascularized organ with one quarter of its blood supply from hepatic artery and three-quarters from portal vein. The hepatic sinusoids in enormous quantities are lined with highly fenestrated endothelial cells. This structural arrangement allows plasma to flow freely through the sinusoidal endothelial cells into the space of Disse [18]. Despite the dual blood supply to normal liver parenchyma, hepatic tumors greater than 2 mm, whether primary or metastatic, are almost exclusively supplied by the proliferated hepatoarterial branches [19]. This phenomenon can be supported by postmortem microangiographic findings in the present study (Fig. 2e,e'). The CTC derived from DCE-MRI (Fig. 3) also indicates similar blood perfusion levels in liver parenchyma with dual blood supply and in RIF-1 tumor solely with arterial supply, suggesting hypervascular nature of this tumor model.

The reason why RIF-1 did not grow in three mice could be attributed to the individual variance of immunity towards this tumor allograft among non-immunocompromised C3H/Km mice, whereas the only intraperitoneal mass found in one mouse could be due to falling of the implanted fragment from the original site into abdominal cavity.

The present liver tumor model may offer certain advantages: (1) compared with subcutaneous implantation, it is more clinically relevant in terms of a more common tumor location; (2) unlike more disseminated liver lesions with cell suspension inoculation [20], a well-defined solitary tumor growth created by tissue fragment implantation may ease the observation and documentation during experiments on new diagnostics and therapeutics; (3) as a result of the ideal liver microenvironment, the composition of virtually homogenous viable tumor cells may avoid possible confusion between spontaneous and therapeutic necrosis if anticancer treatments are investigated; (4) a cycle of 2 weeks for tumor growth facilitates high throughput research in contrast to chemically or physically induced tumor models, which often take months in mice with a higher mortality rate; (5) the observed hypervascular feature of intrahepatic RIF-1 growth may ensure an ample access of the studied diagnostic or therapeutic agents to the tumor, hence more reliable analytical outcomes. Recently, using the present murine liver tumor model, we have successfully evaluated a new imaging marker for identification of tissue viability after a number of cancer interventional therapies [21, 22].

Noninvasive imaging of mouse liver tumors

Characterization of a rat liver tumor model using a clinical MRI scanner has been recently reported [9]. Compared to a rat, the dimension of a mouse is even more than ten times smaller, which posed a greater challenge for us to apply a clinical 1.5-T magnet dedicated to humans that is 3,000-times heavier than a mouse. However, the present study has demonstrated that multiparametric MRI evaluation of liver tumors in mice using a standard clinical MRI machine without additional hardware and software accessories turned out to be feasible with the imaging quality comparable to that with rats [9]. Although the use of 1.5-T clinical MRI scanners for scanning mice has been reported, none of these studies focused on the intrahepatic tumors [23–25].

One of the advantages for using a clinical magnet is the fact that the outcomes obtained from the MRI sequences frequently applied in the clinic, including TSE-T2WI, SE-T1WI, DWI, and DCE-MRI of T1-VIBE, are directly translational from the experimental results in small animals to clinical practice in human patients. In addition, unlike high-field small animal MRI equipment that is super-sensitive to cardiac and respiratory motion artifacts, the lower field strength clinical magnets are much less susceptible to these artifacts in small animals, hence satisfactory imaging quality as demonstrated in this study. Therefore, it seems that a lack of a dedicated small-bore MRI imager should not become an obstacle for certain cancer research studies in mice. For instance, as exemplified in Fig. 4, the dramatic process of initial selective vascular shutdown and subsequent marginal recurrence could be noninvasively documented in mouse liver RIF-1 tumor after systemic administration of the VTA as tested for subcutaneous tumors in rats [16]. Such in vivo morphological and functional evidence is complementary to a previously reported study with only MR spectroscopic measurement [12].

DCE-MRI may provide functional information about vascularity, blood flow and vascular permeability. While DCE-MRI is rarely used in mice with high field magnets [26], DCE-MRI of T1-VIBE was explored for the first time in the present study with a clinical 1.5-T magnet to characterize hemodynamic aspects of the RIF-1 liver tumor. The volume transfer constant, K, is the permeability surface area product per unit volume of tissue [17]. In tumors, the vascular permeability is greater than inflow, so that the delivery of contrast agent to extracellular space is dominated by perfusion, and then the K can be thought to approximate tissue blood flow per unit volume [27, 28]. Initial slope of CTC is proportional to the permeability and easiest to compute, and it requires the shortest data acquisitions. In principle, permeability can be determined from the initial slope, which is more robust than K, because it reflects the enhancement degree more directly without assumptions made for the compartment model [15, 28]. In our study, both K and maximal initial slope of RIF-1 tumor were lower than those of normal liver, but the difference was statistically significant only with maximal initial slope.

Study limitations

In this study, only one tumor cell line, i.e., RIF-1, was investigated, which may not be representative of other

more hepatotropic tumor cell lines, such as colorectal cancer [10]. However, the introduced experimental setting in this study should be easily applicable to many other xenograft tumor implantations in immuno-compromised mice or allograft tumor implantations in non-immunocompromised mice depending on what is required by the specific cancer research topics.

There are also certain limitations for using a clinical magnet in mice, and often compromises have to be made, particularly for functional imaging acquisitions. For instance, initially we attempted to acquire DWI with three directions of X, Y, and Z axes and three different b values to calculate the ADC map, but encountered severe geometric distortion. Therefore, DWI with only one b value and a single direction were chosen, considering balanced anatomic information and contrast between tumor and normal liver tissue. Consequently, the tumor was well demarcated, and the minute necrosis could be detected on DWI. The possibility for further improvement is evident, since ADC maps for subcutaneous tumors in mice have been successfully acquired using different 1.5-T clinical MRI equipment [25]. More measurements with different b values in three different directions are needed to calculate ADC maps, as a novel functional indicator for tissue properties, including viability [16]. This can be realized by further optimization of acquisition parameters in our

setting. Furthermore, in DCE-MRI, the K and maximal initial slope from the normal liver were actually acquired as summed outcomes contributed from both the portal vein and hepatic artery due to the limited temporal resolution of DCE-MRI at 3.8 s per measurement, which is too long to make the dual-path contrast arrivals differentiated in mice (Fig. 3). Besides, the imaging quality with T1-VIBE could be improved if the breathholding was applied in this study.

In conclusion, liver implantation of RIF-1 tumor in mice as a model for solitary malignancy in a visceral organ proves feasible and reproducible. This model can be noninvasively monitored and characterized by multipara-metric MRI using a clinical 1.5-T imager. The present experimental platform can be used as a robust tool to study new diagnostic and therapeutic regimens in cancer research.

References

1. Hann B, Balmain A (2001) Building 'validated' mouse models of human cancer. Curr Opin Cell Biol 13:778–784
2. Kerbel RS (1998) What is the optimal rodent model for anti-tumor drug testing? Cancer Metastasis Rev 17:301–304
3. Bhujwalla ZM, Tozer GM, Field SB et al (1990) The combined measurement of blood flow and metabolism in RIF-1 tumours in vivo. A study using H2 flow and 31P NMR spectroscopy. NMR Biomed 3:178–183
4. Chen HH, Le Visage C, Qiu B et al (2005) MR imaging of biodegradable polymeric microparticles: a potential method of monitoring local drug delivery. Magn Reson Med 53:614–620
5. Kim S-G, Ackerman JJH (1988) Quantitative determination of tumor blood flow and perfusion via deuterium nuclear magnetic resonance spectroscopy in mice. Cancer Res 48:3449–3453
6. Robinson SP, van den Boogaart A, Maxwell RJ (1998) ^{31}P-magnetic resonance spectroscopy and ^{2}H-magnetic resonance imaging studies of a panel of early-generation transplanted murine tumour models. Br J Cancer 77:1752–1760

7. Tailor DR, Poptani H, Glickson JD et al (2003) High-resolution assessment of blood flow in murine RIF-1 tumors by monitoring uptake of $H_2^{17}O$ with proton $T_{1\rho}$-weighted imaging. Magn Reson Med 49:1–6
8. Twentyman PR, Brown JM, Gray JW et al (1980) A new mouse tumor model system (RIF-1) for comparison of end-point studies. J Natl Cancer Inst 64:595–604
9. Chen F, Sun X, De Keyzer F et al (2006) Liver tumor model with implanted rhabdomyosarcoma in rats: MR imaging, microangiography, and histopathologic analysis. Radiology 239:554–562
10. Heijstek MW, Kranenburg O, Borel Rinkes IH (2005) Mouse models of colorectal cancer and liver metastases. Dig Surg 22:16–25
11. Rusciano D, Lorenzoni P, Burger M (1994) Murine models of liver metastasis. Invasion Metastasis 14:349–361
12. Madhu B, Waterton JC, Griffiths JR (2006) The response of RIF-1 fibrosarcomas to the vascular-disrupting agent ZD6126 assessed by in vivo and ex vivo ^{1}H magnetic resonance spectroscopy. Neoplasia 8:560–567

13. Takehara Y, Sakahara H, Masunaga H (2002) Assessment of a potential tumor-seeking manganese metalloporphyrin contrast agent in a mouse model. Magn Reson Med 47:549–553
14. Nomura K, Miyagawa S, Harada H (1998) Relationship between doubling time of liver metastases from colorectal carcinoma and residual primary cancer. Dig Surg 15:21–24
15. Tofts PS, Berkowitz BA (1993) Rapid measurement of capillary permeability using the early part of the dynamic Gd-DTPA MRI enhancement curve. J Magn Reson B 102:129–136
16. Thoeny HC, De Keyzer F, Vandecaveye V (2005) Effect of vascular targeting agent in rat tumor model: dynamic contrast-enhanced versus diffusion-weighted MR imaging. Radiology 237:492–499
17. Tofts PS (1997) Modeling tracer kinetics in dynamic Gd-DTPA MR imaging. J Magn Reson Imaging 7:91–101
18. Pandharipande PV, Krinsky GA, Rusinek H et al (2005) Perfusion imaging of the liver: Current challenges and future goals. Radiology 234:661–673

19. Liu Y, Matsui O (2007) Changes of intratumoral microvessels and blood perfusion during establishment of hepatic metastases in mice. Radiology 243:386–395

20. Veenendaal LM, van Hillegersberg R, Smakman N et al (2006) Synergistic effect of interstitial laser coagulation and doxorubicin in a murine tumor recurrence model of solitary colorectal liver metastasis. Ann Surg Oncol 13:168–175

21. Van de Putte M, Wang H, Chen F, de Witte P, Ni Y (2008) Hypericin as a marker for determination of tissue viability after intratumoral ethanol injection in a murine liver tumor model. Academic Radiology 15(1):107–113

22. Van de Putte M, Wang H, Chen F, de Witte P, Ni Y (2008) Hypericin as a marker for determination of tissue viability after radiofrequency ablation in a murine liver tumor model. Oncology Reports 19, in press

23. Bock NA, Konyer NB, Henkelman RM (2003) Multiple-mouse MRI. Magn Reson Med 49(1):158–167

24. Xu S, Gade TP, Matei C et al (2003) In vivo multiple-mouse imaging at 1.5 T. Magn Reson Med 49(3):551–557

25. Herneth AM, Guccione S, Bednarski M (2003) Apparent Diffusion Coefficient: a quantitative parameter for in vivo tumor characterization. Eur J Radiol 45:208–213

26. Crokart N, Jordan BF, Baudelet C et al (2005) Early reoxygenation in tumors after irradiation: Determining factors and consequences for radiotherapy regimens using daily multiple fractions. Int J Radiat Oncol Biol Phys 63:901–910

27. Collins DJ, Padhani AR (2004) Dynamic magnetic resonance imaging of tumor perfusion. Approaches and biomedical challenges. IEEE Eng Med Biol Mag 23:65–83

28. Tofts PS, Brix G, Buckley DL (1999) Estimating kinetic parameters from dynamic contrast-enhanced T1-weighted MRI of a diffusable tracer: standardized quantities and symbols. J Magn Reson Imaging 10:223–232